Stochastic Maxwell-Bloch equations for modeling amplified spontaneous emission

Jeong-Wan Park [1,*] Kwang-Je Kim [1,2] and Ryan Lindberg [1]
[1]*Argonne National Laboratory, Lemont, Illinois 60439, USA*
[2]*University of Chicago, Chicago, Illinois 60637, USA*

(Received 8 May 2023; accepted 29 July 2024; published 22 August 2024)

An approach for studying atom-radiation interaction has been developed, associating quantum operators with stochastic variables governed by discrete Heisenberg equations. This framework models general multilevel atomic systems using the paraxial approximation in both single- and multipass configurations. Simulation results for x-ray laser oscillators with parameters of interest are presented. The stochastic model is efficient to solve, as the required computational resources scale linearly with the number of emitters, and it may be applicable to various other quantum systems.

DOI: 10.1103/PhysRevA.110.023724

I. INTRODUCTION

Successful observations of transient gain in atomic media [1–4], achieved through inner-shell photoionization by powerful x-ray free electron lasers (XFELs) [5–7], have shown that x-ray lasers may be possible using the physical process variously referred to as superradiance [8], superfluorescence [9,10], and amplified spontaneous emission (ASE) [11]. An x-ray laser oscillator (XLO) [12], a multipass device employing an x-ray cavity [13,14], has been proposed to achieve higher coherence and stability.

To develop a practical XLO, solid understanding and interpretation of experimental outcomes are fundamental, as they lay the groundwork for refining theoretical frameworks and designing experiments with greater accuracy. At the heart of this endeavor is an accurate ASE numerical simulation based on a detailed quantum representation of spontaneous emission in the x-ray domain, where the timescales of radiation are closely aligned with those of loss and decay processes. Additionally, it must account for three-dimensional (3D) effects to adequately model both the spatial dependence of the gain and the diffractive effects of the field. Moreover, it should be adaptable to implementation in systems with multiple turns.

Several theoretical models for simulating ASE have been proposed: The first is based on classical Maxwell-Bloch equations (CMBEs) with an *ad hoc* noise term for the spontaneous emission. They have been used in the past for modeling ASE at optical wavelengths [15] and, more recently, at x-ray wavelengths [4,16–26]. The classical model appears to be suitable in the stimulated-emission-dominant regime, but it fails to accurately predict the time dependence of spontaneous-emission intensity due to its inclusion of random noise in the atomic coherence's time derivative. This results in an initial behavior mimicking Brownian motion and a time-delayed peak [24,27], diverging from the exponential decay predicted by Weisskopf-Wigner theory [28] and confirmed by experiments [29].

Another stochastic model is the positive-P stochastic equations (PPSEs) [30–33], which are based on the positive-P representation [34,35] formulation of quantum mechanics. This method claims to precisely model spontaneous emission's temporal correlation [31,33]. However, the implementation of this approach is typically plagued by divergent solutions to its stochastic equations [31,36,37], which are likely due to the manner in which Hermiticity of the stochastic variables is not maintained [36]. These concerns related to the equations' stability [38–44] partially explain the relatively limited adoption of PPSEs as a numerical tool in quantum optics [34]. Unproven remedies like the stochastic drift gauge transformation [31] introduce distortions, marring the statistical accuracy of ASE modeling [36,45]. An attempt to enforce Hermiticity and mitigate the divergence through perturbative treatment of the stochastic component in the coherence Bloch equation [36] contradicts PPSEs' intrinsic diffusion gauge criteria [31], neglecting the predominantly stochastic nature of all the terms, including decay, in the spontaneous-emission-dominant regime.

Another reduced theoretical model is the one-dimensional (1D) factorized correlation function equations (FCFEs) [27], which are derived by truncating the quantum Maxwell-Bloch equations (QMBEs) through a targeted factorization strategy. This approach results in a self-contained set of differential equations renowned for their precision in predicting spontaneous-emission intensity. However, the significant computational requirements across all combinations of atomic pairings, coupled with the neglect of the dynamics of sequential turns or the 3D diffraction effects, limit their effectiveness for comprehensive XLO simulations.

Here, we propose another approximate approach based on quantum mechanics with which modeling of multipass ASE is straightforward [46]. This approach translates the QMBEs into a set of difference equations, which we refer to as stochastic Maxwell-Bloch equations (SMBEs), by introducing stochastic c-number variables that take the place of corresponding quantum operators. Three-dimensional effects are incorporated via the paraxial approximation.

*Contact author: jeongwan.park@anl.gov

A crucial aspect of developing a stochastic model for ASE is determining how the stochastic nature is integrated into the physical variables. This strategy is normally guided by the quantum characteristics targeted for capture in the stochastic framework, such as the intensity of spontaneous emission for CMBEs and the master equation for PPSEs. For SMBEs, this involves the atomic matrix identities.

SMBEs not only fulfill all the essential criteria for describing weakly correlated quantum systems but can also be implemented in a numerically stable and efficient manner and are, unlike other stochastic models, consistent with the FCFEs. Using the SMBEs, we develop a simulation program for the XLO that incorporates the physics of both ASE and cavity propagation and present some simulation results for parameters of current interest.

II. QUANTUM MAXWELL-BLOCH EQUATIONS

We consider the two-level atomic system with excited and ground states denoted as $|e\rangle^{(a)}$ and $|g\rangle^{(a)}$, respectively, which have an energy difference of $\hbar\Omega$. For simplicity, we assume that the electric dipole transition-matrix element is real and has a magnitude of μ, oriented in $\hat{x}$. This direction is orthogonal to the propagation direction of the pump field, $\hat{z}$. The Hamiltonian for the system is given by [28] (the superscripts label atom a)

$$H = \sum_a \frac{1}{2}\hbar\Omega\sigma_z^{(a)} + \sum_{\mathbf{k},s}\hbar\omega_{\mathbf{k}}a_{\mathbf{k},s}^\dagger a_{\mathbf{k},s} - \mu\sum_a(\sigma_+^{(a)}E_+^{(a)} + E_-^{(a)}\sigma_-^{(a)}), \tag{1}$$

where the positive-frequency electric field is

$$E_+^{(a)}(t) = \sum_{\mathbf{k},s}\mathscr{E}_{\mathbf{k},s}e^{i\mathbf{k}\cdot\mathbf{r}_a}a_{\mathbf{k},s}(t), \tag{2}$$

with its conjugation $E_-^{(a)}(t) = E_+^{(a)\dagger}(t)$. $a_{\mathbf{k},s}^\dagger$ and $a_{\mathbf{k},s}$ are the creation and annihilation operators for photons with wave vector $\mathbf{k}$, frequency $\omega_{\mathbf{k}} = ck$, and polarization index s, and $\mathbf{r}_a$ is the position of atom a. $\mathscr{E}_{\mathbf{k},s} = \sqrt{\frac{\hbar\omega_k}{2\varepsilon_0 V}}\hat{\mathbf{x}}\cdot\hat{\mathbf{e}}_{\mathbf{k},s}$, where $\hat{\mathbf{e}}_{\mathbf{k},s}$ is the unit vector of the field's $\mathbf{k}$ component for the s polarization and V is the quantization volume. The notations of [28] and SI units are used throughout this paper. The atomic operators are

$$\sigma_+^{(a)} = |e\rangle^{(a)}\langle g|^{(a)}, \quad \sigma_-^{(a)} = |g\rangle^{(a)}\langle e|^{(a)}, \tag{3}$$

$$\sigma_{ee}^{(a)} = |e\rangle^{(a)}\langle e|^{(a)} = \sigma_+^{(a)}\sigma_-^{(a)}, \tag{4}$$

$$\sigma_{gg}^{(a)} = |g\rangle^{(a)}\langle g|^{(a)} = \sigma_-^{(a)}\sigma_+^{(a)}, \tag{5}$$

$$\sigma_z^{(a)} = \sigma_{ee}^{(a)} - \sigma_{gg}^{(a)} = 2\sigma_{ee}^{(a)} - 1. \tag{6}$$

Here, $\sigma_z^{(a)}$, $\sigma_+^{(a)}$, and $\sigma_-^{(a)}$ are atom a's operators for inversion, raising, and lowering, respectively.

From the Hamiltonian in Eq. (1), with Eq. (2), we get the following equation of motion for the annihilation operator:

$$\frac{da_{\mathbf{k},s}}{dt} = -i\omega_{\mathbf{k}}a_{\mathbf{k},s}(t) + \frac{i\mu}{\hbar}\mathscr{E}_{\mathbf{k},s}^*\sum_b e^{-i\mathbf{k}\cdot\mathbf{r}_b}\sigma_-^{(b)}(t). \tag{7}$$

Its integration, combined with Eq. (2), yields the electric field:

$$E_+^{(a)}(t) = \sum_{\mathbf{k},s}\mathscr{E}_{\mathbf{k},s}a_{\mathbf{k},s}(0)e^{-i\omega_{\mathbf{k}}t+i\mathbf{k}\cdot\mathbf{r}_a} + \sum_{\mathbf{k},s,b}\frac{i\mu}{\hbar}|\mathscr{E}_{\mathbf{k},s}|^2 \times\int_0^t dt'\, e^{-i\omega_{\mathbf{k}}(t-t')+i\mathbf{k}\cdot(\mathbf{r}_a-\mathbf{r}_b)}\sigma_-^{(b)}(t'). \tag{8}$$

The discrete sum over $\mathbf{k}$ is approximated by

$$\sum_{\mathbf{k}} \to \frac{V}{8\pi^3}\int d^3\mathbf{k} \to \frac{V}{8\pi^3}\int_0^\infty k^2dk\int_0^\pi \sin\theta d\theta\int_0^{2\pi} d\varphi, \tag{9}$$

where θ represents the polar angle and φ denotes the azimuthal angle of the vector $\mathbf{k}$ with respect to the z axis along the medium's length, and the position vector is written as $\mathbf{r} = (\mathbf{x}, z)$, where $\mathbf{x} = (x, y)$ is the transverse part. We introduce $\lambda_\Omega = 2\pi/k_\Omega$ and $k_\Omega = \Omega/c$. Then we write $k = k_\Omega + \Delta k$ and note that for interactions near the atomic transition frequency Ω the main contribution to the k integration comes from the region $\Delta k \ll k_\Omega$, so we introduce a slowly varying envelope description, $\tilde{E}_+^{(a)}(\tau) = e^{i\Omega\tau}E_+^{(a)}(\tau)$ and $\tilde{\sigma}_-^{(a)}(\tau) = e^{i\Omega\tau}\sigma_-^{(a)}(\tau)$, employing the retarded time $\tau = t - z_b/c$ to account for the propagation delay associated with the spatial positioning of atom b [27].

We decompose Eq. (8) into two components:

$$\tilde{E}_+^{(a)}(\tau) = \frac{i\hbar}{2\mu}\Gamma_{\rm sp}\tilde{\sigma}_-^{(a)}(\tau) + \tilde{E}_{+,\rm ext}^{(a)}(\tau). \tag{10}$$

The first term is the self-field of atom a originating from the $b = a$ term in the atomic summation, which is computed with the Weisskopf-Wigner approximation [28] (see the details in Appendix A), where we introduced the spontaneous-emission rate $\Gamma_{\rm sp} \equiv \frac{\mu^2}{3\pi\varepsilon_0\hbar}(\frac{\Omega}{c})^3$. The remaining $\tilde{E}_{+,\rm ext}^{(a)}(\tau)$ denotes the external field acting on atom a, which is split into two parts:

$$\tilde{E}_{+,\rm ext}^{(a)}(\tau) = \tilde{E}_{+,\rm seed}^{(a)}(\tau) + \tilde{E}_{+,\rm ind}^{(a)}(\tau), \tag{11}$$

where $\tilde{E}_{+,\rm seed}^{(a)}(\tau)$ is the seed field containing $a_{\mathbf{k},s}(t=0)$ and $\tilde{E}_{+,\rm ind}^{(a)}(\tau)$ is the field induced by the interactions with all other atoms in the system, corresponding to the $b \neq a$ terms in the sum.

We consider the case where an atomic medium is pumped by XFEL radiation of narrow divergence around the z axis. Thus, the interaction volume is a "thin pencil" of length L and radius R satisfying $\lambda_\Omega \ll R \ll L$. To compute $\tilde{E}_{+,\rm ind}^{(a)}(\tau)$, we change the angular integration in Eq. (9) to that over transverse angles $\boldsymbol{\phi} = (\phi_x, \phi_y)$, which can be interpreted as performing a Fourier transform from $\boldsymbol{\phi}$ space at each k value. In the thin-pencil configuration, significant contributions to the integration arise only from region $\boldsymbol{\phi}_R$, where $|\boldsymbol{\phi}| \ll 1$; contributions from waves that significantly deviate from or counterpropagate against the pump direction are negligible. This observation allows us to apply the *paraxial approximation*, narrowing down the integration

region to the $\boldsymbol{\phi}_R$ as

$$\int d^3\mathbf{k} \to \int_0^\infty k^2 dk \int_{\boldsymbol{\phi}\in\boldsymbol{\phi}_R} d^2\boldsymbol{\phi}. \tag{12}$$

Under the paraxial approximation, the wave vector $\mathbf{k}$ is approximated as $k(\boldsymbol{\phi}, 1-|\boldsymbol{\phi}|^2/2)$. $\tilde{E}^{(a)}_{+,\mathrm{ind}}(\tau)$ then becomes (see the details in Appendix A)

$$\tilde{E}^{(a)}_{+,\mathrm{ind}}(\tau) = i\frac{3\hbar\Gamma_{\mathrm{sp}}}{8\pi\mu}\sum_{b<a}\mathcal{G}(\mathbf{r}_a-\mathbf{r}_b)\tilde{\sigma}^{(b)}_-(\tau), \tag{13}$$

where

$$\mathcal{G}(\mathbf{r}) = \int_{-\infty}^{\infty} d^2\boldsymbol{\phi}\, e^{i\frac{\Omega}{c}\left(\boldsymbol{\phi}\cdot\mathbf{x}-\frac{\phi^2}{2}z\right)} = \frac{\lambda_\Omega}{iz}e^{i\frac{\pi\mathbf{x}^2}{\lambda_\Omega z}} \tag{14}$$

is the paraxial approximation of the far-field Green's function [47]. Due to the particular way the approximation was applied, the dependence on the longitudinal variable τ factors out, and the 3D equations have the same structure as those in one dimension [27]. Equation (13) becomes the 1D version obtained in [27] if we replace $\mathcal{G}$ by a constant solid angle Δo [48].

The equations of motion for the atomic variables are

$$\frac{d\sigma^{(a)}_-(t)}{dt} = -i\Omega\sigma^{(a)}_-(t) - \frac{i\mu}{\hbar}\sigma^{(a)}_z(t)E^{(a)}_+(t), \tag{15}$$

$$\frac{d\sigma^{(a)}_z(t)}{dt} = \frac{2i\mu}{\hbar}[\sigma^{(a)}_+(t)E^{(a)}_+(t) - E^{(a)}_-(t)\sigma^{(a)}_-(t)]. \tag{16}$$

With Eq. (10), the corresponding equations for the slowly varying envelope become

$$\frac{d\tilde{\sigma}^{(a)}_-(\tau)}{d\tau} = -\frac{\Gamma_{\mathrm{sp}}}{2}\tilde{\sigma}^{(a)}_- - \frac{i\mu}{\hbar}\sigma^{(a)}_z\tilde{E}^{(a)}_{+,\mathrm{ext}}, \tag{17}$$

$$\frac{d\sigma^{(a)}_{ee}(\tau)}{d\tau} = -\Gamma_{\mathrm{sp}}\sigma^{(a)}_{ee} + \frac{i\mu}{\hbar}\left[\tilde{\sigma}^{(a)}_+\tilde{E}^{(a)}_{+,\mathrm{ext}} - \tilde{E}^{(a)}_{-,\mathrm{ext}}\tilde{\sigma}^{(a)}_-\right]. \tag{18}$$

The quantity $\sigma^{(a)}_z$ is slowly varying and does not need a tilde. Equations (11), (13), (17), and (18) constitute the QMBEs.

III. FACTORIZED CORRELATION FUNCTION EQUATIONS

If all operators in the QMBEs are replaced by their ensemble averages, the QMBEs reduce to the CMBEs:

$$\tilde{E}^{(a)}_{+,\mathrm{ext}} \to \left\langle\tilde{E}^{(a)}_{+,\mathrm{ext}}\right\rangle = \mathcal{E}^{(a)}_+, \qquad \tilde{\sigma}^{(a)}_+ \to \langle\tilde{\sigma}^{(a)}_+\rangle = \rho^{(a)}_{ge},$$
$$\sigma^{(a)}_{ee} \to \left\langle\sigma^{(a)}_{ee}\right\rangle = \rho^{(a)}_{ee}, \qquad \sigma^{(a)}_z \to \left\langle\sigma^{(a)}_z\right\rangle = \rho^{(a)}_{\mathrm{inv}}. \tag{19}$$

Here, $\rho^{(a)}_{\mathrm{inv}} = \rho^{(a)}_{ee} - \rho^{(a)}_{gg}$, $\rho^{(a)}_{ij}$ is the (i,j)th element of the atomic density matrix $\rho^{(a)}$, and the off-diagonal elements $\rho^{(a)}_{eg}$ and $\rho^{(a)}_{ge}$ are known as "coherence." To model ASE within the framework of the CMBEs, it is necessary to add an *ad hoc* noise term as shown in [25] to mimic spontaneous emission.

A possible quantum-mechanical approach is to develop equations for a hierarchy of multipoint correlation functions, beginning with the ensemble average, denoted by angular brackets, in Eq. (11):

$$\begin{aligned}\mathcal{E}^{(a)}_+(\tau) &\equiv \left\langle\tilde{E}^{(a)}_{+,\mathrm{ext}}(\tau)\right\rangle \\ &= \mathcal{E}^{(a)}_{+,\mathrm{seed}}(\tau) \\ &\quad + i\frac{3\hbar\Gamma_{\mathrm{sp}}}{8\pi\mu}\sum_{b<a}\mathcal{G}(\mathbf{r}_a-\mathbf{r}_b)\langle\tilde{\sigma}^{(b)}_-(\tau)\rangle,\end{aligned} \tag{20}$$

where $\mathcal{E}^{(a)}_{+,\mathrm{seed}} = \langle\tilde{E}^{(a)}_{+,\mathrm{seed}}\rangle$ is the incoming seed field. The ensemble averages of Eqs. (17) and (18) are

$$\left\langle\frac{d\tilde{\sigma}^{(a)}_-}{d\tau}\right\rangle = -\frac{\Gamma_{\mathrm{sp}}}{2}\langle\tilde{\sigma}^{(a)}_-\rangle - \frac{i\mu}{\hbar}\left\langle\sigma^{(a)}_z\tilde{E}^{(a)}_{+,\mathrm{ext}}\right\rangle, \tag{21}$$

$$\begin{aligned}\left\langle\frac{d\sigma^{(a)}_{ee}}{d\tau}\right\rangle &= -\Gamma_{\mathrm{sp}}\left\langle\sigma^{(a)}_{ee}\right\rangle \\ &\quad + \frac{i\mu}{\hbar}\left\langle\tilde{\sigma}^{(a)}_+\tilde{E}^{(a)}_{+,\mathrm{ext}} - \tilde{E}^{(a)}_{-,\mathrm{ext}}\tilde{\sigma}^{(a)}_-\right\rangle.\end{aligned} \tag{22}$$

Since the right-hand side of Eq. (22) contains two point correlation functions $\langle\tilde{\sigma}^{(a)}_+\tilde{\sigma}^{(b)}_-\rangle$, for $a\neq b$, we need to consider their evolution equations, obtained with Eq. (17):

$$\begin{aligned}\left\langle\frac{d(\tilde{\sigma}^{(a)}_+\tilde{\sigma}^{(b)}_-)}{d\tau}\right\rangle &= -\Gamma_{\mathrm{sp}}\langle\tilde{\sigma}^{(a)}_+\tilde{\sigma}^{(b)}_-\rangle \\ &\quad + \frac{i\mu}{\hbar}\left\langle\tilde{E}^{(a)}_{-,\mathrm{ext}}\sigma^{(a)}_z\tilde{\sigma}^{(b)}_- - \tilde{\sigma}^{(a)}_+\sigma^{(b)}_z\tilde{E}^{(b)}_{+,\mathrm{ext}}\right\rangle.\end{aligned} \tag{23}$$

The right-hand side of this equation now contains three-point correlation functions *ad infinitum*, reflecting the Bogoliubov-Born-Green-Kirkwood-Yvon hierarchy of reduced density-matrix equations [27,49]. To close the system with a finite number of correlation functions, the following factorization ansatz may be imposed for $a\neq b$:

$$\left\langle\sigma^{(a)}_z\tilde{\sigma}^{(b)}_\pm\right\rangle \to \left\langle\sigma^{(a)}_z\right\rangle\langle\tilde{\sigma}^{(b)}_\pm\rangle, \tag{24}$$

$$\left\langle\tilde{\sigma}^{(c)}_+\sigma^{(a)}_z\tilde{\sigma}^{(b)}_-\right\rangle \to \left\langle\sigma^{(a)}_z\right\rangle\langle\tilde{\sigma}^{(c)}_+\tilde{\sigma}^{(b)}_-\rangle, \quad a\neq c. \tag{25}$$

Assuming that the seed field factorizes, the system of equations (20)–(23), referred to as FCFEs, is now closed for the quantities $\langle\sigma^{(a)}_z\rangle$, $\langle\tilde{\sigma}^{(a)}_\pm\rangle$, and $\langle\tilde{\sigma}^{(a)}_+\tilde{\sigma}^{(b)}_-\rangle$ and provides an approximate description of the quantum-mechanical evolution of ASE. For an interaction volume containing N atoms, there are N^2+N quantities to compute. The 1D FCFEs were introduced and studied in [27].

Within the framework of FCFEs, ensemble averages $\langle\tilde{E}^{(a)}_{+,\mathrm{ext}}(\tau)\rangle$ and $\langle\tilde{E}^{(a)}_{-,\mathrm{ext}}(\tau)\tilde{E}^{(a)}_{+,\mathrm{ext}}(\tau)\rangle$ are computed instead of the field operator $\tilde{E}^{(a)}_{+,\mathrm{ext}}(\tau)$. To model a multipass ASE such as an XLO, however, the field operator at the end of a pass is necessary to serve as the input for the next pass. Therefore, FCFEs cannot be the basis for modeling XLO.

IV. STOCHASTIC MAXWELL-BLOCH EQUATIONS

In our pursuit of a refined model for simulating multipass ASE, we introduce a set of SMBEs. These equations enhance the CMBEs by incorporating certain quantum dynamics that are encoded in the QMBEs but typically lost in the transition to CMBEs.

We begin by noting that the positive-frequency far-field operator of spontaneous emission from an isolated atom b is

proportional to $\sigma_-^{(b)}$ [28,47]. The intensity of the spontaneous emission is then proportional to

$$\langle \tilde{\sigma}_+^{(b)} \tilde{\sigma}_-^{(b)} \rangle = \langle \sigma_{ee}^{(b)} \rangle. \tag{26}$$

Here, we used the operator identity (4). Equation (26) implies that the term $\langle \tilde{\sigma}_+^{(c)} \tilde{\sigma}_-^{(b)} \rangle$ in Eq. (25) cannot be factorized as $\langle \tilde{\sigma}_+^{(c)} \rangle \langle \tilde{\sigma}_-^{(b)} \rangle$ because c can be equal to b.

The basic insight in SMBEs is that it is possible to modify the CMBEs so that the structure of Eq. (26) is preserved by adding a stochastic term to the coherence. Since the phase of the stochastic term changes abruptly from one instant to the next, a precise formulation of SMBEs is only possible with discrete time steps $\tau_n = n\Delta\tau$. At each time step for each atom, we assign a random phase $\Phi_{(n)}^{(a)}$, which can take any value in the interval $(0, 2\pi]$. The probability distributions at different time steps and for different atoms are independent. Therefore,

$$\overline{\exp\left(i\Phi_{(n)}^{(a)} - i\Phi_{(m)}^{(b)}\right)} = \delta_{ab}\delta_{nm}, \tag{27}$$

where the bar denotes averaging over *all* possible phases.

The SMBEs are formulated inductively as follows: assume that $\rho_{ge(n)}^{(a)}$, $\rho_{eg(n)}^{(a)}$, $\rho_{ee(n)}^{(a)}$, and $\rho_{gg(n)}^{(a)}$ are given at n for all a. The stochastic coherence is defined by (the stacked notation in this paper's equations succinctly represents two related but distinct equations; the upper elements denote one set of equations, while the lower elements denote another set)

$$\hat{\rho}_{\substack{ge \\ eg(n)}}^{(a)} = \rho_{\substack{ge \\ eg(n)}}^{(a)} + \xi_{\substack{ge \\ eg(n)}}^{(a)}, \tag{28}$$

where the stochastic terms are

$$\xi_{\substack{ge \\ eg(n)}}^{(a)} = \sqrt{\rho_{ee(n)}^{(a)} - \rho_{ge(n)}^{(a)}\rho_{eg(n)}^{(a)}}\, e^{\pm i\Phi_{(n)}^{(a)}}. \tag{29}$$

It follows from Eqs. (28) and (29) that

$$\overline{\hat{\rho}_{ge(n)}^{(c)}\hat{\rho}_{eg(n)}^{(b)}}^{\{n\}} = \rho_{ge(n)}^{(c)}\rho_{eg(n)}^{(b)} + \delta_{cb}\left(\rho_{ee(n)}^{(b)} - \rho_{ge(n)}^{(b)}\rho_{eg(n)}^{(b)}\right). \tag{30}$$

The qualifier $\{n\}$ at the end of the bar signifies that the averaging is only for the phases at the time step n. Complying with Eq. (13), we write

$$\begin{aligned}
\hat{\mathcal{E}}_{+(n)}^{(a)} &= \mathcal{E}_{+,\mathrm{seed}(n)}^{(a)} + i\frac{3\hbar\Gamma_{\mathrm{sp}}}{8\pi\mu}\sum_{b<a}\mathcal{G}(\mathbf{r}_a - \mathbf{r}_b)\hat{\rho}_{eg(n)}^{(b)}, \\
\hat{\mathcal{E}}_{-(n)}^{(a)} &= \mathcal{E}_{-,\mathrm{seed}(n)}^{(a)} - i\frac{3\hbar\Gamma_{\mathrm{sp}}}{8\pi\mu}\sum_{b<a}\mathcal{G}(\mathbf{r}_b - \mathbf{r}_a)\hat{\rho}_{ge(n)}^{(b)}.
\end{aligned} \tag{31}$$

The stochastic quantities $\hat{\mathcal{E}}_{\pm(n)}^{(a)}$ correspond to the electric field operators $\tilde{E}_{\pm,\mathrm{ext}}^{(a)}(\tau_n)$.

Quantities for the next time step $n+1$ are determined by converting the QMBEs to difference equations. In doing this, we interpret an equation of the form $\frac{d\mathcal{O}}{d\tau} = \mathcal{U}(\tau)$ as

$$\overline{(\mathcal{O}_{(n+1)} - \mathcal{O}_{(n)})}^{\{n+1\}} = \Delta\tau\,\overline{\mathcal{U}_{(n)}}^{\{n+1\}}. \tag{32}$$

This averaging does not affect quantities at time step n, but $\overline{\hat{\rho}_{\substack{ge \\ eg(n+1)}}^{(a)}}^{\{n+1\}} = \rho_{\substack{ge \\ eg(n+1)}}^{(a)}$. We obtain

$$\begin{aligned}
\rho_{ee(n+1)}^{(a)} &= \rho_{ee(n)}^{(a)} + \left\{r_{e(n)}^{(a)} - \Gamma_{ee(n)}^{(a)}\rho_{ee(n)}^{(a)} + \frac{i\mu}{\hbar}\left[\hat{\rho}_{ge(n)}^{(a)}\hat{\mathcal{E}}_{+(n)}^{(a)} - \hat{\mathcal{E}}_{-(n)}^{(a)}\hat{\rho}_{eg(n)}^{(a)}\right]\right\}\Delta\tau, \\
\rho_{gg(n+1)}^{(a)} &= \rho_{gg(n)}^{(a)} + \left\{r_{g(n)}^{(a)} + \left(\Gamma_{\mathrm{sp}} + \gamma_n\right)\rho_{ee(n)}^{(a)} - \gamma_{g(n)}^{(a)}\rho_{gg(n)}^{(a)} - \frac{i\mu}{\hbar}\left[\hat{\rho}_{ge(n)}^{(a)}\hat{\mathcal{E}}_{+(n)}^{(a)} - \hat{\mathcal{E}}_{-(n)}^{(a)}\hat{\rho}_{eg(n)}^{(a)}\right]\right\}\Delta\tau, \\
\rho_{\substack{ge \\ eg(n+1)}}^{(a)} &= \hat{\rho}_{\substack{ge \\ eg(n)}}^{(a)} + \left[-\frac{\Gamma_{(n)}^{(a)}}{2}\hat{\rho}_{\substack{ge \\ eg(n)}}^{(a)} \pm \frac{i\mu}{\hbar}\hat{\mathcal{E}}_{\mp(n)}^{(a)}\rho_{\mathrm{inv}(n)}^{(a)}\right]\Delta\tau.
\end{aligned} \tag{33}$$

Above, we have incorporated incoherent processes using the Lindblad superoperator method, introducing the following rates [27]: $\Gamma^{(a)}(\tau) \equiv \Gamma_{ee}^{(a)}(\tau) + \gamma_g^{(a)}(\tau) + q^{(a)}(\tau)$ and $\Gamma_{ee}^{(a)}(\tau) \equiv \Gamma_{\mathrm{sp}} + \gamma_e^{(a)}(\tau) + \gamma_n$, where γ_n is the nonradiative decay rate, q is the rate for atom decoherence, r_e and r_g are the pumping rates for the excited and ground states, and γ_e and γ_g are the depletion rates. The incoherent processes act differently on $\rho_{ee}^{(a)}$ and $\rho_{gg}^{(a)}$, and we need separate equations for them. The inductive procedure is finally completed by determining $\hat{\rho}_{ge(n+1)}^{(a)}$, $\hat{\rho}_{eg(n+1)}^{(a)}$, $\hat{\mathcal{E}}_{+(n+1)}^{(a)}$, and $\hat{\mathcal{E}}_{-(n+1)}^{(a)}$ by replacing n by $n+1$ in Eqs. (28) and (31), respectively, and introducing new random phases $\Phi_{(n+1)}^{(a)}$ for all atoms a. Equations (28), (31), and (33) constitute SMBEs.

The variables $\hat{\rho}_{ge(n)}^{(a)}$, $\hat{\rho}_{eg(n)}^{(a)}$, $\rho_{ee(n)}^{(a)}$, and $\rho_{gg(n)}^{(a)}$ are the stochastic c numbers corresponding to the quantum operators $\tilde{\sigma}_+^{(a)}(\tau_n)$, $\tilde{\sigma}_-^{(a)}(\tau_n)$, $\sigma_{ee}^{(a)}(\tau_n)$, and $\sigma_{gg}^{(a)}(\tau_n)$, respectively. They are used to compute the ensemble average of operators and *normally ordered* second-order operator products in terms of the coherence [28]. The ensemble average in the framework of the SMBEs is obtained by averaging over all stochastic phases. Thus, for example,

$$\langle \sigma_{ee(n)}^{(a)} \rangle = \overline{\rho_{ee(n)}^{(a)}}, \quad \langle \tilde{\sigma}_{+(n)}^{(a)} \tilde{\sigma}_{-(n)}^{(b)} \rangle = \overline{\hat{\rho}_{ge(n)}^{(a)}\hat{\rho}_{eg(n)}^{(b)}}. \tag{34}$$

Equation (26) then follows from Eq. (30), as promised:

$$\langle \tilde{\sigma}_{+(n)}^{(a)} \tilde{\sigma}_{-(n)}^{(a)} \rangle = \overline{\hat{\rho}_{ge(n)}^{(a)}\hat{\rho}_{eg(n)}^{(a)}} = \overline{\rho_{ee(n)}^{(a)}} = \langle \sigma_{ee(n)}^{(a)} \rangle. \tag{35}$$

Note the stochastic variables are *not* to be used to compute the ensemble average of reverse-ordered second-order products. Thus, for example, $\overline{\hat{\rho}_{eg(n)}^{(a)}\hat{\rho}_{ge(n)}^{(b)}}$ does not correspond to $\langle \tilde{\sigma}_{-(n)}^{(a)} \tilde{\sigma}_{+(n)}^{(b)} \rangle$. SMBEs can be extended to multilevel atoms, as explained in Appendix B.

Another key characteristic of the field is its spectral profile, which is derived from the Fourier transform of the temporal field correlation function. Since SMBEs determine the $\overline{\hat{\rho}_{\substack{ge \\ eg(n)}}^{(a)}}$, they also govern the correlation, according to the quantum regression theorem [28].

The SMBEs lead to an approximate factorization that resembles Eqs. (24) and (25) in the sense that $\overline{\rho^{(a)}_{\mathrm{inv(n)}}\hat{\rho}^{(b)}_{ge(n)}}^{\{n\}} = \rho^{(a)}_{\mathrm{inv(n)}}\overline{\hat{\rho}^{(b)}_{ge(n)}}^{\{n\}}$ and $\overline{\rho^{(a)}_{\mathrm{inv(n)}}\hat{\rho}^{(b)}_{ge(n)}\hat{\rho}^{(c)}_{eg(n)}}^{\{n\}} = \rho^{(a)}_{\mathrm{inv(n)}}\overline{\hat{\rho}^{(b)}_{ge(n)}\hat{\rho}^{(c)}_{eg(n)}}^{\{n\}}$ for $a \neq b, c$. However, $\rho^{(a)}_{\mathrm{inv(n)}}$ contains a term $\hat{\rho}^{(d)}_{eg(m)}$, and $\hat{\rho}^{(b)}_{ge(n)}$ contains a term $\hat{\rho}^{(d)}_{ge(m)}$ for $m < n$. After averaging over all phases, these two terms will contract to $\rho^{(d)}_{ee(m)}$ in view of Eq. (35). Therefore, the factorization ansatz adopted in FCFEs, Eqs. (24) and (25), does not hold for the SMBEs; nevertheless, the closed set of differential equations of FCFEs in terms of the atomic variables can be derived from the SMBEs by forcefully applying this ansatz, as shown in Appendix C.

For SMBEs, preserving the second-order atomic matrix identities in Eq. (35), which are also maintained by FCFEs, is crucial for obtaining the closed set of equations of FCFEs, as shown in Appendix C. In contrast, CMBEs and PPSEs do not demonstrate consistency with FCFEs in preserving these identities. Unlike SMBEs, PPSEs use distinct stochastic variables for atomic coherence and field source terms, leading to nonzero stochastic sources even in the absence of atoms. In the spontaneous-emission-dominant regime, such PPSEs result in vanishing ensemble averages of atomic coherence products from an atom [31], thus not preserving Eq. (35). The inability of CMBEs and PPSEs with the stochastic drift gauge transformation to correctly predict the intensity of spontaneous emission, as given by the closed set of equations of FCFEs, implies an inconsistency with the closed set.

The simple case of a single atom without the incoming field and other incoherent processes, except for the pumping and spontaneous emission, is instructive. We may suppress the atomic label and set $\hat{\mathcal{E}}_{\pm(n)} = 0$. The initial values are $\rho_{\substack{ge\\eg}(0)}$, $\rho_{ee(0)}$, $\hat{\rho}_{\substack{ge\\eg}(0)} = \rho_{\substack{ge\\eg}(0)} + \xi_{\substack{ge\\eg}(0)}$, and $\xi_{\substack{ge\\eg}(0)} = \sqrt{\rho_{ee(0)} - \rho_{ge(0)}\rho_{eg(0)}}e^{\pm i\Phi_{(0)}}$. For $n \geqslant 1$, we find

$$\rho_{ee(n)} = \sum_{m=1}^{n} X^{n-m} r_{e(m-1)}\Delta\tau + X^n \rho_{ee(0)}, \tag{36}$$

$$\hat{\rho}_{\substack{ge\\eg}(n)} = \sum_{m=1}^{n} X_h^{n-m}\xi_{\substack{ge\\eg}(m)} + X_h^n \hat{\rho}_{\substack{ge\\eg}(0)}, \tag{37}$$

$$\overline{\xi_{ge(m)}\xi_{eg(m)}} = r_{e(m-1)}\Delta\tau,\ m \geqslant 1. \tag{38}$$

Here, $X = 1 - \Gamma_{\mathrm{sp}}\Delta\tau \approx e^{-\Gamma_{\mathrm{sp}}\Delta\tau}$, and $X_h = 1 - \frac{1}{2}\Gamma_{\mathrm{sp}}\Delta\tau \approx e^{-\Gamma_{\mathrm{sp}}\Delta\tau/2}$ for a small time step $\Delta\tau \ll \Gamma_{\mathrm{sp}}^{-1}$. The excited-state population ρ_{ee} and the stochastic coherence $\hat{\rho}_{\substack{ge\\eg}}$ decay exponentially as $e^{-\Gamma_{\mathrm{sp}}\tau}$ and $e^{-\Gamma_{\mathrm{sp}}\tau/2}$, respectively, the former replenished by pumping and the latter by the stochastic term $\xi_{\substack{ge\\eg}(m)}$. The temporal correlation for $l \geqslant n$ is

$$\overline{\hat{\rho}_{ge(n)}\hat{\rho}_{eg(l)}} = \rho_{ee(n)}e^{-\frac{\Gamma_{\mathrm{sp}}}{2}(l-n)\Delta\tau}, \tag{39}$$

in agreement with $\langle\tilde{\sigma}_+(\tau_n)\tilde{\sigma}_-(\tau_l)\rangle$, as expected. The positive-frequency far field is proportional to $\hat{\rho}_{eg(n)}$. By computing its Poynting vector [28], one can check that the number of photons emitted is equal to the initial excitation $\rho_{ee(0)}$ in the absence of pumping.

V. NUMERICAL EXAMPLES

We shall present some numerical simulations with SMBEs. An XLO simulation starts by setting the ASE initial conditions $\mathcal{E}^{(a)}_{\pm,\mathrm{seed}(0)} = 0$ and $\rho^{(a)}_{\substack{ge\\eg}(0)} = 0$. Subsequently, the simulation computes $\hat{\mathcal{E}}^{(a)}_{\pm(n)}$ with a given set of phases $\{\Phi^{(c)}_{(m)}\}$ for all atoms and all time steps in the first pass. The output is then used as the input to the next round of the XLO calculation.

For numerical calculations, we adopted the continuous description that offers advantages by replacing the discrete atomic label with the average position of atoms $\mathbf{r}$ within a small volume ΔV surrounding the atom. This is mathematically represented as

$$\rho^{(\mathbf{r})}_{(n)} \equiv \frac{1}{n_v\Delta V}\sum_{a\in\Delta V}\rho^{(a)}_{(n)}. \tag{40}$$

Here, n_v denotes the 3D number density of the atoms. In this framework, field calculations at position $\mathbf{r}$ are carried out using the differential form of Eq. (31), with detailed explanations provided in Appendix D. The transition to continuous representation for the difference equations is achieved by substituting the discrete atomic label with the continuous position variable in the discrete difference equations in Eq. (33). Additional details of the continuous noise representation, Eqs. (E6) and (E7), which starts with an inductive formula for Eq. (29) designed to mitigate potential numerical instabilities associated with its exact form and facilitate the transition to the continuous representation, are elaborated in Appendix E. We implemented the Runge-Kutta fourth-order method for the difference equations. Details on the equations governing the pumping rate are provided in Appendix F.

We have verified that the radiation intensity from 1D SMBEs obtained by substituting $\mathcal{G}$ with the solid angle $\Delta o = \pi R^2/L^2$ closely aligns with the corresponding intensity plot from the 1D FCFEs presented in Fig. 3(a) of [27], using the parameters specified therein. This close match may suggest that the factorization ansatz applied in the FCFEs introduces minimal distortions in this scenario.

To compare our SMBE simulations with those that use either the CMBEs with a 3D *ad hoc* noise term [25,50] or the PPSEs [31], we adopt simulation parameters close to those of the XLO designed in [12]. In this case the lasing medium was chosen to be a jet of cupric nitrate, while the transition is given by the copper's $K\alpha_1$ decay channel that is created when the XFEL pump creates a $1s$ core hole. Detailed parameters are $\lambda_\Omega = 0.154$ nm, $\Gamma_{\mathrm{sp}}^{-1} = 1.10$ fs, $\gamma_e^{-1} = 0.70$ fs, $\gamma_g^{-1} = 1.18$ fs, $L = 270$ μm, $n_v = 4.2\times10^{27}$ m^{-3}, $r_g = q = \gamma_n = 0$, photoionization cross section of pumping to the excited state $\sigma_{\mathrm{abs}} = 32.4$ kb, and a 9-keV pump pulse with Gaussian longitudinal ($\sigma_\tau = 8.49$ fs) and transverse (focused for σ_r of 0.1 μm at the waist, situated at the midpoint of medium) profiles. Numerical resolutions in the medium are $\Delta\tau = 43$ as in a 60-fs grid, $\Delta x = \Delta y = 16.7$ nm in a 1×1 μm^2 grid, and $\Delta z = 0.54$ μm.

A. Spontaneous emission

Before conducting simulations for the designed laser, we initially simulated the spontaneous emission to assess the accuracy of the three different models in depicting the temporal intensity profile. For this test, we disabled all incoherent processes except for spontaneous emission. The atoms were initially set to a fully excited state, and the simulations were

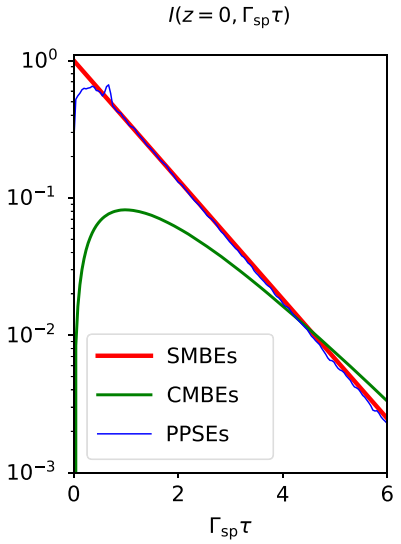

FIG. 1. Temporal intensity profile of spontaneous emission, averaged over 10^3 sets of phase samples and normalized to the initial intensity of SMBEs.

carried out at $z \simeq 0$, where the effect of stimulated emission is negligible. The results are presented in Fig. 1.

The SMBE curve correctly exhibits the expected exponential decay as $e^{-\Gamma_{sp}\tau}$, confirming its suitability for these conditions. In contrast, the CMBE curve displays the incorrect decay pattern, $\Gamma_{sp}\tau e^{-\Gamma_{sp}\tau}$, as previously noted [24,27]. The PPSE curve also shows some inaccuracies at early times, which we primarily attribute to the way that the stochastic drift gauge transformation is used to control divergent trajectories when there is a population inversion in the medium.

B. Single-pass laser

Using the parameters set for the designed machine, our next step was to simulate the single-pass case. In Figs. 2 and 3, where the pump is centered at 30 fs, we plot the SMBEs' radiation intensity profiles with the pump pulse delivering

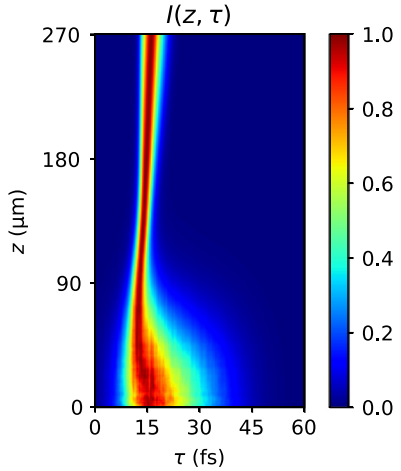

FIG. 2. SMBEs' radiation intensity profiles from a set of phase samples in the laser, normalized to the maximum at each z.

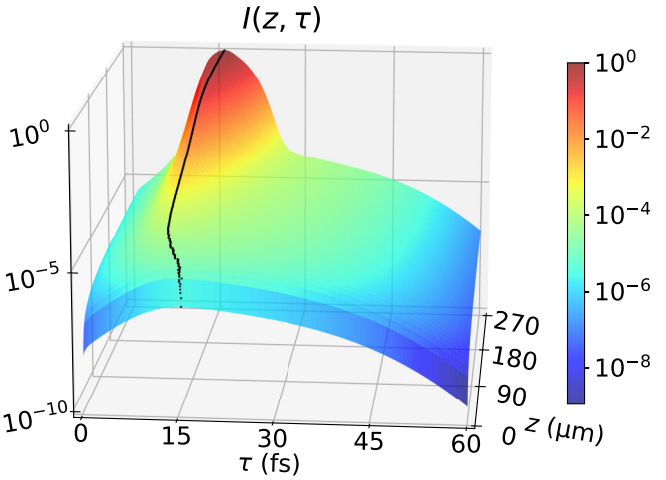

FIG. 3. SMBEs' radiation intensity profiles in the laser, averaged over 10^3 sets of phase samples and normalized to the overall maximum (the black dots represent the maximum at each z).

1.3×10^{12} photons. Figure 2, which is *not* phase averaged, shows the fluctuation of spontaneous emission at smaller z values, which diminishes as z increases into the stimulated-emission-dominant regime. Figure 3, averaged over 10^3 sets of phase samples, clearly delineates the transition from the spontaneous-emission-dominant regime to the stimulated-emission-dominant regime.

Figure 4, also averaged over 10^3 sets of phase samples, distinctly illustrates the varying model predictions under low-intensity pumping conditions, indicated by solid lines. This highlights how the inaccuracies in the other models regarding the modeling of spontaneous-emission intensity, as elaborated in Sec. V A, contribute to the discrepancies in representing the behavior of actual lasers compared to our SMBEs. In the case of PPSEs, under conditions of population inversion where the stochastic drift gauge transformation distorts radiation intensity, lasing is significant, which may explain the notable discrepancy. In scenarios of high-intensity pumping, represented by dashed lines, although the models initially present distinct predictions at the medium's entrance, they

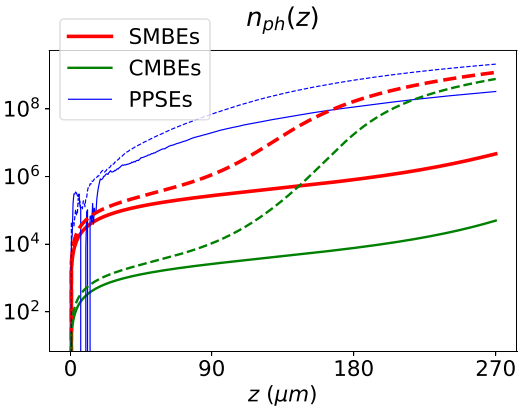

FIG. 4. Radiated photon numbers for pump pulse with 2.0×10^{11} (solid lines) and 1.3×10^{12} (dashed lines) photons in the laser.

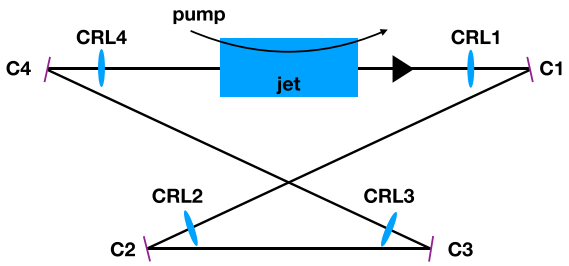

FIG. 5. Outline of the cavity for XLO.

tend to converge due to the predominant influence of stimulated emission towards the medium's end.

C. Multipass XLO

The next simulation we conducted is the multipass XLO. Considering the cavity design in [12], we implemented a four-bounce bow-tie cavity configuration $(+--+)$ [51] using Si(444) crystals, as illustrated in Fig. 5, in the simulation. Each crystal with a Bragg angle of 79.3° at the resonance energy exhibits 1% loss, with Gaussian Bragg FWHM values of 31.6 μrad and 48.1 meV. The cavity includes the pump, the atomic jet, and compound refractive lenses (CRLs) with a focal length of 1.29 cm and measures 50 cm in length. The jet's center is positioned at the center of the upper horizontal branch where the transverse mode size is aligned with the pump size. CRL1 is placed 1.4 cm away from the jet's center, before the first crystal, C1, to reduce the angular divergence.

In Fig. 6, we present the results showing the radiated photon number as a function of the turn number [52,53], averaged over 30 sets of phase samples. In the high-intensity pumping case, represented by the dashed lines, the profiles of the SMBEs and CMBEs are practically indistinguishable, while PPSEs show a slightly reduced net cavity gain per turn and saturation power. Hence, in this case all models predict a gain

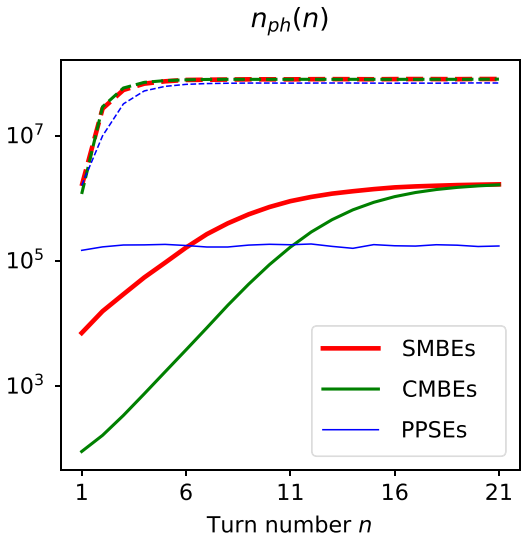

FIG. 6. Number of radiated photons in XLO (after cavity propagation, before entering the jet) for the low-intensity (solid line) and high-intensity (dashed lines) pumpings.

and saturation power that is close to that of the Maxwell-Bloch equations and further show similar levels of initial seeding by ASE.

On the other hand, the three models have rather distinct photon-number predictions in the low-intensity pumping case, plotted as solid lines. Nevertheless, the gain and saturation power of the SMBEs and CMBEs are quite similar in this scenario. The main difference between the SMBEs' and CMBEs' predictions is in regard to the photon number produced in the initial passes, which results from the differing treatment of the spontaneous emission that serves to seed the oscillator. Hence, while the SMBEs and CMBEs would lead to similar predictions regarding the steady-state performance of an XLO, they may provide differing conclusions for the feasibility of an XLO driven by a small number of pump pulses. The PPSEs yield entirely different predictions in the low-intensity pumping case, with its solid line showing no effective gain. Hence, it appears that the PPSEs predict a reduction in the small-signal gain from that of SMBEs or perhaps that the spontaneous emission otherwise modifies the stimulated emission.

To summarize, Fig. 6 shows that all three models give similar results when the pumping is strong and spontaneous emission is relatively unimportant, while they yield increasingly different predictions as the pump becomes weaker and the role of spontaneous emission becomes correspondingly stronger. In our opinion, the agreement between SMBEs and FCFEs, as demonstrated in Appendix C and the 1D simulation comparison mentioned above, lends increased confidence to the SMBEs' results. Moreover, it is unlikely that CMBEs and PPSEs, which cannot correctly describe the experimentally observed exponential decay of spontaneous emission, can be reliable when these discrepancies in predictions are pronounced.

VI. CONCLUSION

We introduced an approach to ASE using the stochastic Maxwell-Bloch equations, which establish a connection between stochastic dynamic variables and the quantum operators of the Maxwell-Bloch system. We showed how to incorporate second-order atomic matrix identities into the SMBEs, thereby ensuring numerical stability and accurate predictions of first-order field correlations for ASE. This makes the SMBEs an effective tool for precisely modeling general atomic systems within the paraxial approximation for both single- and multipass configurations. In contrast, the existing stochastic models, which do not correctly incorporate the second-order identities, struggle to model ASE accurately in the spontaneous-emission-dominant regime, which can be crucial for multiturn configurations. Even when a system is assumed to be in the stimulated-emission-dominant regime, these models may need to reference predictions from an accurate theory to verify the transition to the regime from the spontaneous-emission-dominant regime and the resulting improved accuracy, which may limit their practicality.

In systems with a large number of emitters, such as XLO, the second-order atomic matrix identities primarily govern higher-order correlations of the field. Consequently, the SMBEs may accurately capture also these higher-order correlations in large systems, which is relevant to leveraging

quantum features such as intensity interferometry. This contrasts with smaller systems, in which the quantum behavior of individual emitters becomes more significant and relevant to quantum technologies. Future refinements of SMBEs, focusing on integrating higher-order atomic matrix identities, have the potential to enhance the accuracy of these equations, particularly for the smaller systems [54].

This stochastic framework, which aligns with Heisenberg's matrix mechanics, could find applications for a variety of quantum phenomena. By integrating critical quantum matrix identities into a stochastic framework, it provides a tool whose numerical requirements scale linearly with the size of the system. This simplification may help foster innovative methodologies and deepen the understanding of quantum mechanics across other fields beyond quantum optics.

ACKNOWLEDGMENTS

We wish to thank K. Li and L. Young at the University of Chicago for introducing the physics of x-ray interaction and propagation through an atomic medium pumped by an XFEL and Y. Li and G. Tiwari for useful advice on streamlining the simulation. This work is supported by the U.S. Department of Energy, Office of Science, under Contract No. DE-AC02-06CH11357.

APPENDIX A: SELF-FIELD AND $\tilde{E}^{(a)}_{+,\mathrm{ind}}(\tau)$ COMPUTATIONS

The self-field, the first term on the right-hand side of Eq. (10), is from the $b = a$ term in the summation of Eq. (8):

$$\begin{aligned}
&\sum_{\mathbf{k},s} i\frac{\mu}{\hbar}|\mathscr{E}_{\mathbf{k},s}|^2 \\
&\quad\times\int_0^{\tau+\frac{z_a}{c}} d\tau' e^{i\Omega\tau - i\omega_{\mathbf{k}}\left(\tau+\frac{z_a}{c}-\tau'\right)}\sigma_-^{(b)}\left(\tau'-\frac{z_a}{c}\right) \\
&= \frac{i\mu}{16\pi^3\epsilon_0}\int_0^{\pi}\int_0^{2\pi}(\cos^2\varphi+\cos^2\theta\sin^2\varphi)d\varphi\sin\theta d\theta \\
&\quad\times\int_{-\frac{z_a}{c}}^{\tau} d\tau'\int_0^{\infty} e^{-i(\omega_k-\Omega)(\tau-\tau')}\tilde{\sigma}_-^{(a)}(\tau')\omega_k k^2 dk \\
&= \frac{i\mu}{3\pi\epsilon_0}\left(\frac{\Omega}{c}\right)^3\int_{-\frac{z_a}{c}}^{\tau}\delta(\tau-\tau')\tilde{\sigma}_-^{(a)}(\tau')d\tau' \\
&= \frac{i\hbar}{2\mu}\Gamma_{\mathrm{sp}}\tilde{\sigma}_-^{(a)}(\tau). \qquad \text{(A1)}
\end{aligned}$$

Here, we used $\hat{\mathbf{e}}_{\mathbf{k},1} \parallel (\cos\varphi, \sin\varphi, 0)$ and $\hat{\mathbf{e}}_{\mathbf{k},2} \parallel (-\sin\varphi\cos\theta, \cos\varphi\cos\theta, \sin\theta)$. Arriving at the second-to-last equality, we used the approximation typically done in the Weisskopf-Wigner approach and introduced the spontaneous-emission rate $\Gamma_{\mathrm{sp}} \equiv \frac{\mu^2}{3\pi\varepsilon_0\hbar}(\frac{\Omega}{c})^3$.

Next, we compute $\tilde{E}^{(a)}_{+,\mathrm{ind}}(\tau)$ in Eq. (11), with the paraxial approximation:

$$\begin{aligned}
\tilde{E}^{(a)}_{+,\mathrm{ind}}(\tau) &= \sum_{\mathbf{k},s} i\frac{\mu}{\hbar}|\mathscr{E}_{\mathbf{k},s}|^2\sum_{b\neq a}\int_{-\frac{z_b}{c}}^{\tau+\frac{z_a-z_b}{c}} d\tau_b \\
&\quad\times e^{-ic\Delta k\mathcal{T}_{ab}+i\Phi_{ab}}\tilde{\sigma}_-^{(b)}(\tau_b) \\
&\simeq \frac{ic\mu}{16\pi^3\epsilon_0}\int_0^{\infty}k^3dk\int_{\boldsymbol{\phi}\in\boldsymbol{\phi}_R}d^2\boldsymbol{\phi}\sum_{b\neq a} \\
&\quad\times\int_{-\frac{z_b}{c}}^{\tau+\frac{z_a-z_b}{c}} d\tau_b\, e^{-ic\Delta k\mathcal{T}_{ab}+i\Phi_{ab}}\tilde{\sigma}_-^{(b)}(\tau_b), \qquad \text{(A2)}
\end{aligned}$$

where

$$\mathcal{T}_{ab} = \tau - \tau_b - \boldsymbol{\phi}\cdot\frac{\mathbf{x}_a-\mathbf{x}_b}{c}, \qquad \text{(A3)}$$

$$\Phi_{ab} = -k_\Omega\frac{|\boldsymbol{\phi}|^2}{2}(z_a-z_b) + k_\Omega\boldsymbol{\phi}\cdot(\mathbf{x}_a-\mathbf{x}_b). \qquad \text{(A4)}$$

We note that the phase in Eq. (A2) varies rapidly and the integration is approximately zero unless $\Delta k \simeq 0$. Hence, we proceed in a manner similar to the Weisskopf-Wigner approximation by replacing k with k_Ω everywhere except for in the fast-oscillating term and by extending the limits of the k integration to be from $-\infty$ to ∞. Then, the k integration results in a δ function, and Eq. (A2) becomes

$$\begin{aligned}
\tilde{E}^{(a)}_{+,\mathrm{ind}}(\tau) &\simeq \frac{i\mu k_\Omega^3}{8\pi^2\epsilon_0}\sum_{b\neq a}\int_{\boldsymbol{\phi}\in\boldsymbol{\phi}_R}d^2\boldsymbol{\phi}\, e^{i\Phi_{ab}} \\
&\quad\times\int_{-\frac{z_b}{c}}^{\tau+\frac{z_a-z_b}{c}} d\tau_b\,\tilde{\sigma}_-^{(b)}(\tau_b)\delta(\mathcal{T}_{ab}). \qquad \text{(A5)}
\end{aligned}$$

We approximate the argument of a δ function, $\mathcal{T}_{ab} \simeq \tau - \tau_b$, with the following condition that usually holds for a numerical computation with z resolution of Δz:

$$|\boldsymbol{\phi}| \ll \min\left(\frac{z_a-z_b}{|\mathbf{x}_a-\mathbf{x}_b|}\right) \sim \frac{\Delta z}{2R}. \qquad \text{(A6)}$$

Then Eq. (A5) is approximated as

$$\begin{aligned}
\tilde{E}^{(a)}_{+,\mathrm{ind}}(\tau) &= i\frac{3\hbar\Gamma_{\mathrm{sp}}}{8\pi\mu}\int_{\boldsymbol{\phi}\in\boldsymbol{\phi}_R}d^2\boldsymbol{\phi}\sum_{b<a}\tilde{\sigma}_-^{(b)}(\tau) \\
&\quad\times e^{ik_\Omega[\boldsymbol{\phi}\cdot(\mathbf{x}_a-\mathbf{x}_b)-\frac{\boldsymbol{\phi}^2}{2}(z_a-z_b)]}, \qquad \text{(A7)}
\end{aligned}$$

where $b < a$ is shorthand notation for $z_b < z_a$. The summation over $\mathbf{x}_b$ with the same z_b can be regarded as the transverse integration. Then approximately only integrands for $|\boldsymbol{\phi}| \ll \frac{\lambda_\Omega}{2R}$ contribute substantially to the $\boldsymbol{\phi}$ integration. Therefore, approximately, we can change the limits of the $\boldsymbol{\phi}$ integration to be from $-\infty$ to ∞; then $\tilde{E}^{(a)}_{+,\mathrm{ind}}(\tau)$ becomes Eq. (13).

APPENDIX B: SMBEs FOR MULTILEVEL SYSTEMS

SMBEs can be effectively adapted to accommodate multilevel atomic systems. Each interacting pair of two energy levels is designated by an index α, labeling the corresponding upper $|e_\alpha\rangle$ and lower $|g_\alpha\rangle$ energy states and the atomic operators. Similar to the matrix identity in Eq. (26) for the two-level system, an analogous identity exists for the ordered set of (α, β) pairs that governs the spontaneous-emission intensity. This identity, represented by Eq. (B1), should therefore be preserved by the stochastic coherences $\hat{\rho}_{g_\alpha e_\alpha}$ and $\hat{\rho}_{e_\beta g_\beta}$:

$$\left\langle\tilde{\sigma}_{+_\alpha}^{(b)}\tilde{\sigma}_{-_\beta}^{(b)}\right\rangle = \delta_{g_\alpha g_\beta}\left\langle\tilde{\sigma}_{e_\beta e_\alpha}^{(b)}\right\rangle, \qquad \text{(B1)}$$

where $\sigma^{(b)}_{e_\beta e_\alpha} = |e_\alpha\rangle^{(b)}\langle e_\beta|^{(b)}$ and $\delta_{g_\alpha g_\beta}$ is 1 if the two lower-energy states coincide and 0 otherwise. The noise terms satisfying this are

$$\xi^{(a)}_{g_\alpha e_\alpha(n)} = \sum_\beta \sqrt{\delta_{g_\alpha g_\beta}\rho^{(a)}_{e_\beta e_\alpha(n)} - \rho^{(a)}_{g_\alpha e_\alpha(n)}\rho^{(a)}_{e_\beta g_\beta(n)}}\, e^{i\Phi^{(a)}_{\alpha\beta(n)}},$$
$$\xi^{(a)}_{e_\alpha g_\alpha(n)} = \sum_\beta \sqrt{\delta_{g_\alpha g_\beta}\rho^{(a)}_{e_\alpha e_\beta(n)} - \rho^{(a)}_{g_\beta e_\beta(n)}\rho^{(a)}_{e_\alpha g_\alpha(n)}}\, e^{-i\Phi^{(a)}_{\beta\alpha(n)}}, \tag{B2}$$

where the random phases satisfy

$$\overline{\exp\left(i\Phi^{(a)}_{\alpha\beta(n)} - i\Phi^{(b)}_{\alpha'\beta'(m)}\right)} = \delta_{ab}\delta_{nm}\delta_{\alpha\alpha'}\delta_{\beta\beta'}. \tag{B3}$$

Limiting the summation in Eq. (B2) to the $\beta = \alpha$ term as an approximation is justifiable because, in the spontaneous-emission-dominant regime where the field is negligible and noise plays a significant role, this approach preserves the required identity of the SMBEs corresponding to Eq. (B1).

APPENDIX C: THE CLOSED SET OF DIFFERENTIAL EQUATIONS OF FCFEs OBTAINED FROM SMBEs

From the SMBEs' difference equation in Eq. (33) and with the noise factors from Eq. (29), we derive the following for distinct atoms $a \neq b$:

$$\hat\rho^{(a)}_{ge(n+1)}\hat\rho^{(b)}_{eg(n+1)} = \left(\hat\rho^{(a)}_{ge(n)} + \xi^{(a)}_{ge(n+1)}\right)\left(\hat\rho^{(b)}_{eg(n)} + \xi^{(b)}_{eg(n+1)}\right) + \left(\hat\rho^{(a)}_{ge(n)} + \xi^{(a)}_{ge(n+1)}\right)\left(-\frac{\Gamma^{(b)}_{(n)}}{2}\hat\rho^{(b)}_{eg(n)} - \frac{i\mu}{\hbar}\hat{\mathcal{E}}^{(b)}_{+(n)}\rho^{(b)}_{\mathrm{inv}(n)}\right)\Delta\tau$$
$$+ \left(\hat\rho^{(b)}_{eg(n)} + \xi^{(b)}_{eg(n+1)}\right)\left(-\frac{\Gamma^{(a)}_{(n)}}{2}\hat\rho^{(a)}_{ge(n)} + \frac{i\mu}{\hbar}\hat{\mathcal{E}}^{(a)}_{-(n)}\rho^{(a)}_{\mathrm{inv}(n)}\right)\Delta\tau. \tag{C1}$$

Upon averaging over all phases, with the inclusion of the field equation, Eq. (31), the expression simplifies to

$$\overline{\hat\rho^{(a)}_{ge(n+1)}\hat\rho^{(b)}_{eg(n+1)}} = \overline{\hat\rho^{(a)}_{ge(n)}\hat\rho^{(b)}_{eg(n)}} - \frac{\Gamma^{(a)}_{(n)} + \Gamma^{(b)}_{(n)}}{2}\overline{\hat\rho^{(a)}_{ge(n)}\hat\rho^{(b)}_{eg(n)}}\Delta\tau$$
$$- \frac{i\mu}{\hbar}\left(\overline{\hat\rho^{(a)}_{ge(n)}\mathcal{E}^{(b)}_{+,\mathrm{seed}(n)}\rho^{(b)}_{\mathrm{inv}(n)}} - \overline{\hat\rho^{(b)}_{eg(n)}\mathcal{E}^{(a)}_{-,\mathrm{seed}(n)}\rho^{(a)}_{\mathrm{inv}(n)}}\right)\Delta\tau$$
$$+ \frac{3\Gamma_{\mathrm{sp}}}{8\pi}\left(\sum_{c<b}\mathcal{G}(\mathbf{r}_b - \mathbf{r}_c)\overline{\hat\rho^{(a)}_{ge(n)}\hat\rho^{(c)}_{eg(n)}\rho^{(b)}_{\mathrm{inv}(n)}} + \sum_{c<a}\mathcal{G}(\mathbf{r}_c - \mathbf{r}_a)\overline{\hat\rho^{(b)}_{eg(n)}\hat\rho^{(c)}_{ge(n)}\rho^{(a)}_{\mathrm{inv}(n)}}\right)\Delta\tau. \tag{C2}$$

If we enforce the factorizations

$$\overline{\hat\rho^{(a)}_{ge(n)}\mathcal{E}^{(b)}_{+,\mathrm{seed}(n)}\rho^{(b)}_{\mathrm{inv}(n)}} = \overline{\hat\rho^{(a)}_{ge(n)}}\,\overline{\mathcal{E}^{(b)}_{+,\mathrm{seed}(n)}}\,\overline{\rho^{(b)}_{\mathrm{inv}(n)}},\ \overline{\hat\rho^{(c)}_{ge(n)}\hat\rho^{(b)}_{eg(n)}\rho^{(a)}_{\mathrm{inv}(n)}} = \overline{\hat\rho^{(c)}_{ge(n)}\hat\rho^{(b)}_{eg(n)}}\,\overline{\rho^{(a)}_{\mathrm{inv}(n)}},\ a \neq c, \tag{C3}$$

which align with FCFEs' factorizations in Eqs. (24) and (25), the resulting equations mirror those for $\langle\tilde\sigma^{(a)}_+\tilde\sigma^{(b)}_-\rangle$ in FCFEs [27]. Similarly, the difference equations for $\overline{\rho^{(a)}_{\mathrm{inv}}}$, $\overline{\hat\rho^{(a)}_{eg}}$, and $\overline{\hat\rho^{(a)}_{ge}}$ also mirror the corresponding difference equations in FCFEs. FCFEs identify that the $b = c$ term, $\overline{\hat\rho^{(b)}_{ge(n)}\hat\rho^{(b)}_{eg(n)}} = \overline{\rho^{(b)}_{ee(n)}}$, is crucial for accurately describing spontaneous emission.

APPENDIX D: DIFFERENTIAL FIELD EQUATIONS IN THE CONTINUOUS POSITION REPRESENTATION

The field equations from Eq. (31) are translated into their differential forms in continuous space as follows [15]:

$$\frac{\partial\hat{\mathcal{E}}^{(\mathbf{r})}_{+(n)}}{\partial z} = -\frac{\kappa^{(\mathbf{r})}}{2}\hat{\mathcal{E}}^{(\mathbf{r})}_{+(n)} + \frac{ic}{2\Omega}\nabla^2_\perp\hat{\mathcal{E}}^{(\mathbf{r})}_{+(n)} + \frac{i\Omega}{2\epsilon_0 c}\mu n_v\hat\rho^{(\mathbf{r})}_{eg(n)},$$
$$\frac{\partial\hat{\mathcal{E}}^{(\mathbf{r})}_{-(n)}}{\partial z} = -\frac{\kappa^{(\mathbf{r})}}{2}\hat{\mathcal{E}}^{(\mathbf{r})}_{-(n)} - \frac{ic}{2\Omega}\nabla^2_\perp\hat{\mathcal{E}}^{(\mathbf{r})}_{-(n)} - \frac{i\Omega}{2\epsilon_0 c}\mu n_v\hat\rho^{(\mathbf{r})}_{ge(n)}. \tag{D1}$$

In this formulation, $\kappa^{(\mathbf{r})}$ represents the spatially dependent absorption coefficient, which is introduced to account for the attenuation of radiation as it propagates through the medium.

APPENDIX E: THE NOISE TERMS IN THE CONTINUOUS POSITION REPRESENTATION

Before proceeding to derive the continuous position representation for the noise terms, we first need to establish an inductive formula for the noise term specified in Eq. (29). Starting with the values of $\rho^{(a)}_{ee(n)}$, $\rho^{(a)}_{gg(n)}$, $\hat{\rho}^{(a)}_{eg(n)}$, and $\hat{\rho}^{(a)}_{ge(n)}$ for all a, which dictate the unhatted values at the next time step $n+1$ via Eq. (33) and fulfill the noise requirement in Eq. (35) at time step n, we derive a $\xi^{(a)}_{\substack{ge\\eg(n+1)}}$ that meets the noise requirement at the next time step $n+1$ as follows, with Eqs. (29) and (33):

$$\xi^{(a)}_{\substack{ge\\eg(n+1)}} = \sqrt{\left[\rho_{ee}(1-\Gamma_{ee}\Delta\tau) - \hat{\rho}_{ge}\hat{\rho}_{eg}(1-\Gamma\Delta\tau) + r_e\Delta\tau + \frac{i\mu}{\hbar}(1+\rho_{\rm inv})\big(\hat{\mathcal{E}}_+\hat{\rho}_{ge} - \hat{\mathcal{E}}_-\hat{\rho}_{eg}\big)\Delta\tau\right]^{(a)}_{(n)}} e^{\pm i\Phi^{(a)}_{(n+1)}}. \tag{E1}$$

After replacing $\hat{\rho}^{(a)}_{ge(n)}\hat{\rho}^{(a)}_{eg(n)}$ with $\rho^{(a)}_{ee(n)}$, which maintains the invariant $\overline{\xi^{(a)}_{ge(n+1)}\xi^{(a)}_{eg(n+1)}}$ and, consequently, $\overline{\hat{\rho}^{(a)}_{ge(n+1)}\hat{\rho}^{(a)}_{eg(n+1)}}$, the simplified expression is

$$\xi^{(a)}_{\substack{ge\\eg(n+1)}} = \sqrt{\left[r_e + \rho_{ee}\big(\gamma_g+q\big) + \frac{i\mu}{\hbar}(1+\rho_{\rm inv})\big(\hat{\mathcal{E}}_+\hat{\rho}_{ge} - \hat{\mathcal{E}}_-\hat{\rho}_{eg}\big)\right]^{(a)}_{(n)}\Delta\tau} e^{\pm i\Phi^{(a)}_{(n+1)}}. \tag{E2}$$

This formula allows inductive calculation of subsequent values, preserving the noise requirement at each time step.

For the transition to continuous representation, first, we perform the transition inside the square root, which maintains the noise requirement at time step $n+1$ due to the relationships specified below:

$$\overline{\rho^{(a)}_{ee(n)}} = \overline{\rho^{(\mathbf{r})}_{ee(n)}}, \quad \overline{\rho^{(a)}_{inv(n)}\hat{\rho}^{(a)}_{eg(n)}\hat{\rho}^{(b)}_{ge(n)}} = \overline{\rho^{(\mathbf{r})}_{inv(n)}\hat{\rho}^{(\mathbf{r})}_{eg(n)}\hat{\rho}^{(\mathbf{r}')}_{ge(n)}}, \tag{E3}$$

where $\mathbf{r}'$ denotes the continuous spatial position corresponding to an atom $b \neq a$ outside the volume ΔV. Then Eq. (E2) becomes

$$\xi^{(a)}_{\substack{ge\\eg(n+1)}} = \sqrt{\left[r_e + \rho_{ee}\big(\gamma_g+q\big) + \frac{i\mu}{\hbar}(1+\rho_{\rm inv})\big(\hat{\mathcal{E}}_+\hat{\rho}_{ge} - \hat{\mathcal{E}}_-\hat{\rho}_{eg}\big)\right]^{(\mathbf{r})}_{(n)}\Delta\tau} e^{\pm i\Phi^{(a)}_{(n+1)}}. \tag{E4}$$

Then, according to Eq. (40), the continuous position representation is

$$\xi^{(\mathbf{r})}_{\substack{ge\\eg(n+1)}} = \sqrt{\left[r_e + \rho_{ee}\big(\gamma_g+q\big) + \frac{i\mu}{\hbar}(1+\rho_{\rm inv})\big(\hat{\mathcal{E}}_+\hat{\rho}_{ge} - \hat{\mathcal{E}}_-\hat{\rho}_{eg}\big)\right]^{(\mathbf{r})}_{(n)}\Delta\tau} \sum_{a\in\Delta V}\frac{e^{\pm i\Phi^{(a)}_{(n+1)}}}{n_v\Delta V}. \tag{E5}$$

This can be modified as follows, which leaves $\overline{\xi^{(\mathbf{r})}_{ge(n+1)}\xi^{(\mathbf{r})}_{eg(n+1)}}$ invariant:

$$\xi^{(\mathbf{r})}_{\substack{ge\\eg(n+1)}} = \sqrt{\left[r_e + \rho_{ee}\big(\gamma_g+q\big) + \frac{i\mu}{\hbar}(1+\rho_{\rm inv})\big(\hat{\mathcal{E}}_+\hat{\rho}_{ge} - \hat{\mathcal{E}}_-\hat{\rho}_{eg}\big)\right]^{(\mathbf{r})}_{(n)}\Delta\tau} \frac{e^{\pm i\Phi^{(\mathbf{r})}_{(n+1)}}}{\sqrt{n_v\Delta V}}. \tag{E6}$$

The random phase $\Phi^{(\mathbf{r})}_{(n)}$ adheres to the property $\overline{e^{i(\Phi^{(\mathbf{r})}_{(n)} - \Phi^{(\mathbf{r}')}_{(m)})}} = \delta_{\mathbf{r}\mathbf{r}'}\delta_{nm}$.

For the simulations presented in this paper, we initialize the system under conditions of no coherence. Accordingly, we use the following expression for the initial time step:

$$\xi^{(\mathbf{r})}_{\substack{ge\\eg(0)}} = \sqrt{\rho^{(\mathbf{r})}_{ee(0)}}\frac{e^{\pm i\Phi^{(\mathbf{r})}_{(0)}}}{\sqrt{n_v\Delta V}}, \tag{E7}$$

as specified by Eq. (29). For subsequent time steps, Eq. (E6) is utilized.

APPENDIX F: THE RATE OF PUMPING BY XFEL

Here, we provide the detailed equation for r_e, the pumping rate for the excited state, as follows [16]:

$$\rho^{(\mathbf{r})}_{xx(n+1)} = \rho^{(\mathbf{r})}_{xx(n)}\big(1 - \sigma_{\rm abs}J^{(\mathbf{r})}_{(n)}\Delta\tau\big), \tag{F1}$$

$$\frac{\partial\mathcal{E}^{(\mathbf{r})}_{p,+(n)}}{\partial z} = i\frac{c}{2\Omega_p}\nabla^2_\perp\mathcal{E}^{(\mathbf{r})}_{p,+(n)} - \frac{\sigma_{\rm abs}n_v}{2}\rho^{(\mathbf{r})}_{xx(n)}\mathcal{E}^{(\mathbf{r})}_{p,+(n)}, \tag{F2}$$

$$r^{(\mathbf{r})}_{e(n)} = \sigma_{\rm abs}\rho^{(\mathbf{r})}_{xx(n)}J^{(\mathbf{r})}_{(n)}, \tag{F3}$$

where $\rho^{(\mathbf{r})}_{xx(n)}$ represents the population of the energy level from which the atoms are excited by the pump. $\sigma_{\rm abs}$ denotes the photoionization cross section of the pumping process, and Ω_p is the angular frequency of the pump field. $J^{(\mathbf{r})}_{(n)} = 2\frac{c\epsilon_0}{\hbar\Omega_p}|\mathcal{E}^{(\mathbf{r})}_{p,+(n)}|^2$ denotes the pump photon number per unit area per unit time, where $\mathcal{E}^{(\mathbf{r})}_{p,+(n)}$ denotes the slowly varying envelope of the pump's positive-frequency field.

[1] M. D. Doyle *et al.*, Seeded stimulated x-ray emission at 5.9 keV, Optica **10**, 513 (2023).

[2] N. Rohringer *et al.*, Atomic inner-shell x-ray laser at 1.46 nanometres pumped by an x-ray free-electron laser, Nature (London) **481**, 488 (2012).

[3] H. Yoneda *et al.*, Atomic inner-shell laser at 1.5-ångström wavelength pumped by an x-ray free-electron laser, Nature (London) **524**, 446 (2015).

[4] T. Kroll *et al.*, Stimulated x-ray emission spectroscopy in transition metal complexes, Phys. Rev. Lett. **120**, 133203 (2018).

[5] T. Ishikawa *et al.*, A compact x-ray free-electron laser emitting in the sub-angstrom region, Nat. Photon. **6**, 540 (2012).

[6] P. Emma *et al.*, First lasing and operation of an angstrom-wavelength free-electron laser, Nat. Photon. **4**, 641 (2010).

[7] W. Decking *et al.*, A MHz-repetition-rate hard x-ray free-electron laser driven by a superconducting linear accelerator, Nat. Photon. **14**, 391 (2020).

[8] R. H. Dicke, Coherence in spontaneous radiation processes, Phys. Rev. **93**, 99 (1954).

[9] R. Bonifacio and L. A. Lugiato, Cooperative radiation processes in two-level systems: Superfluorescence, Phys. Rev. A **11**, 1507 (1975).

[10] R. Bonifacio and L. A. Lugiato, Cooperative radiation processes in two-level systems: Superfluorescence. II, Phys. Rev. A **12**, 587 (1975).

[11] A. Siegman, *Lasers* (University Science Books, Palo Alto, CA, 1986).

[12] A. Halavanau, A. Benediktovitch, A. A. Lutman, D. DePonte, D. Cocco, N. Rohringer, U. Bergmann, and C. Pellegrini, Population inversion x-ray laser oscillator, Proc. Natl. Acad. Sci. USA **117**, 15511 (2020).

[13] K.-J. Kim, Y. Shvyd'ko, and S. Reiche, A proposal for an x-ray free-electron laser oscillator with an energy-recovery linac, Phys. Rev. Lett. **100**, 244802 (2008).

[14] Z. Huang and R. D. Ruth, Fully coherent x-ray pulses from a regenerative-amplifier free-electron laser, Phys. Rev. Lett. **96**, 144801 (2006).

[15] M. Gross and S. Haroche, Superradiance: An essay on the theory of collective spontaneous emission, Phys. Rep. **93**, 301 (1982).

[16] C. Weninger and N. Rohringer, Transient-gain photoionization x-ray laser, Phys. Rev. A **90**, 063828 (2014).

[17] C. Lyu, S. M. Cavaletto, C. H. Keitel, and Z. Harman, Narrow-band hard-x-ray lasing with highly charged ions, Sci. Rep. **10**, 9439 (2020).

[18] A. Depresseux *et al.*, Table-top femtosecond soft x-ray laser by collisional ionization gating, Nat. Photon. **9**, 817 (2015).

[19] Y. Wang *et al.*, Gain dynamics in a soft-x-ray laser amplifier perturbed by a strong injected x-ray field, Nat. Photon. **8**, 381 (2014).

[20] C. Weninger, M. Purvis, D. Ryan, R. A. London, J. D. Bozek, C. Bostedt, A. Graf, G. Brown, J. J. Rocca, and N. Rohringer, Stimulated electronic x-ray Raman scattering, Phys. Rev. Lett. **111**, 233902 (2013).

[21] V. Kimberg and N. Rohringer, Amplified x-ray emission from core-ionized diatomic molecules, Phys. Rev. Lett. **110**, 043901 (2013).

[22] E. Oliva, M. Fajardo, L. Li, M. Pittman, T. T. T. Le, J. Gautier, G. Lambert, P. Velarde, D. Ros, S. Sebban, and P. Zeitoun, A proposal for multi-tens of GW fully coherent femtosecond soft x-ray lasers, Nat. Photonics **6**, 764 (2012).

[23] A. Depresseux *et al.*, Demonstration of a circularly polarized plasma-based soft-x-ray laser, Phys. Rev. Lett. **115**, 083901 (2015).

[24] Š. Krušič, K. Bučar, A. Mihelič, and M. Žitnik, Collective effects in the radiative decay of the 2^1P state in helium, Phys. Rev. A **98**, 013416 (2018).

[25] O. Larroche, D. Ros, A. Klisnick, A. Sureau, C. Möller, and H. Guennou, Maxwell-Bloch modeling of x-ray-laser- signal buildup in single- and double-pass configurations, Phys. Rev. A **62**, 043815 (2000).

[26] E. Oliva, E. V. Fernández-Tello, M. Cotelo, P. M. Gil, J. A. Moreno, and P. Velarde, 3D multi-scale modelling of plasma-based seeded soft x-ray lasers, Eur. Phys. J. D **75**, 290 (2021).

[27] A. Benediktovitch, V. P. Majety, and N. Rohringer, Quantum theory of superfluorescence based on two-point correlation functions, Phys. Rev. A **99**, 013839 (2019).

[28] M. O. Scully and M. S. Zubairy, *Quantum Optics* (Cambridge University Press, Cambridge, 1997).

[29] S. Pucher, P. Schneeweiss, A. Rauschenbeutel, and A. Dareau, Lifetime measurement of the cesium 5 $^2D_{5/2}$ state, Phys. Rev. A **101**, 042510 (2020).

[30] J. J. Maki, M. S. Malcuit, M. G. Raymer, R. W. Boyd, and P. D. Drummond, Influence of collisional dephasing processes on superfluorescence, Phys. Rev. A **40**, 5135 (1989).

[31] S. Chuchurka, A. Benediktovitch, Š. Krušič, A. Halavanau, and N. Rohringer, Stochastic modeling of x-ray superfluorescence, Phys. Rev. A **109**, 033725 (2024).

[32] P. D. Drummond and M. G. Raymer, Quantum theory of propagation of nonclassical radiation in a near-resonant medium, Phys. Rev. A **44**, 2072 (1991).

[33] Š. Krušič, A. Mihelič, K. Bučar, A. Benediktovitch, S. Chuchurka, and M. Žitnik, XUV superfluorescence from helium gas in the paraxial three-dimensional approximation, Phys. Rev. A **107**, 013113 (2023).

[34] A. Gilchrist, C. W. Gardiner, and P. D. Drummond, Postivie P representation: Application and validity, Phys. Rev. A **55**, 3014 (1997).

[35] R. J. Glauber, *Quantum Theory of Optical Coherence* (Wiley, Weinheim, 2007).

[36] S. Chuchurka, V. Sukharnikov, and N. Rohringer, Hermitian stochastic methodology for x-ray superfluorescence, Phys. Rev. A **109**, 063705 (2024).

[37] P. Deuar and P. D. Drummond, First-principles quantum dynamics in interacting Bose gases II: Stochastic gauges, J. Phys. A **39**, 2723 (2006).

[38] M. Dörfle and A. Schenzle, Bifurcations and the positive P-representation, Z. Phys. B **65**, 113 (1986).

[39] S. Sarkar, J. S. Satchell, and H. J. Carmichael, The positive P representation and the laser equations, J. Phys. A **19**, 2765 (1986).

[40] J. S. Satchell and S. Sarkar, Quantisation of limit cycles in a P representation of a dissipative driven anharmonic oscillator, J. Phys. A **19**, 2737 (1986).

[41] A. M. Smith and C. W. Gardiner, Simulations of nonlinear quantum damping using the positive P representation, Phys. Rev. A **39**, 3511 (1989).

[42] I. J. D. Craig and K. J. McNeil, Quantum simulations of nonlinear optical damping: An exact solution for the stochastic

differential equations and an interpretation of "spiking," Phys. Rev. A **39**, 6267 (1989).
[43] K. J. McNeil and I. J. D. Craig, Positive-P representation for second-harmonic generation: Analytic and computational results, Phys. Rev. A **41**, 4009 (1990).
[44] R. Schack and A. Schenzle, Positive P representation, Phys. Rev. A **44**, 682 (1991).
[45] This becomes evident upon implementing the transformation in Eq. (G3) of [31].
[46] J.-W. Park, K.-J. Kim, and R. Lindberg, Noise-modified, paraxial Maxwell-Bloch equations for x-ray amplified spontaneous emission, arXiv:2305.04653.
[47] R. Loudon, *The Quantum Theory of Light*, 3rd ed. (Oxford University Press, Oxford, 2000).
[48] To be consistent, the coefficient in front of the inhomogeneous term in [27] was reduced to one half of that in Eq. (13).
[49] M. Bonitz, The method of reduced density operators, in *Quantum Kinetic Theory*, 2nd ed. (Springer, Cham, 2016), pp. 29–69.
[50] For Δo factor in the noise term in Fig. 1, Δo corresponding to the $\boldsymbol{\phi}$ grid size is used. For the other figures, following [33], $\Delta o = \pi R^2/L^2$ is used ($R \simeq \sqrt{2}\sigma_r$), while using $\Delta o = \lambda_\Omega^2/R^2$, the other common approximation [15,27] produced similar results.
[51] R. M. J. Cotterill, A universal planar x-ray resonator, Appl. Phys. Lett. **12**, 403 (1968).
[52] To minutely resolve the small angular and spectral acceptance of crystals, outside the medium the temporal and transverse resolutions are changed to $\Delta x = \Delta y = 17.7$ nm in a 53.2×15.9 μm^2 grid and $\Delta\tau = 7.50$ fs in a 1.5-ps grid.
[53] For each set of phase samples from SMBEs, at every turn, the output field from the medium almost completely preserved Hermiticity, prompting us to extract only the positive-frequency field, propagate it up to the medium's entrance, and impose Hermiticity on the seed field for the next turn to streamline the simulation.
[54] J.-W. Park, K.-J. Kim, and R. Lindberg (unpublished).